Isotopic effects on phonon anharmonicity in layered van der Waals crystals: Isotopically pure hexagonal boron nitride

Ramon Cusco, Luis Artus, James H. Edgar, Song Liu, Guillaume Cassabois, Bernard Gil

Isotopic effects on phonon anharmonicity in layered van der Waals crystals: A study of isotopically pure hexagonal boron nitride

Ramon Cuscó and Luis Artús

Institut Jaume Almera (ICTJA-CSIC), Consejo Superior de Investigaciones Científicas, Lluís Solé i Sabarís s.n., 08028 Barcelona, Spain

James H. Edgar and Song Liu

Department of Chemical Engineering, Kansas State University, Manhattan, Kansas 66506, USA

Guillaume Cassabois

Laboratoire Charles Coulomb (L2C), UMR 5221 CNRS-Université de Montpellier, F-34095, Montpellier,France

Bernard Gil

Laboratoire Charles Coulomb (L2C), UMR 5221 CNRS-Université de Montpellier, F-34095, Montpellier,France and Ioffe Institute St. Petersburg, Polytekhnicheskaya 26, St. Petersburg, 194021, Russia.

Abstract

Hexagonal boron nitride (h-BN) is a layered crystal that is attracting a great deal of attention as a promising material for nanophotonic applications. The strong optical anisotropy of this crystal is key to exploit polaritonic modes for manipulating light-matter interactions in 2D materials. h-BN has also great potential for solid-state neutron detection and neutron imaging devices, given the exceptionally high thermal neutron capture cross section of the boron-10 isotope. A good knowledge of phonons in layered crystals is essential for harnessing long-lived phonon-polariton modes for nanophotonic applications and may prove valuable for developing solid-state ^{10}BN neutron detectors with improved device architectures and higher detection efficiencies. Although phonons in graphene and isoelectronic materials with a similar hexagonal layer structure have been studied, the effect of isotopic substitution on the phonons of such lamellar compounds has not been addressed yet. Here we present a Raman scattering study of the *in-plane* high-energy Raman active mode on isotopically-enriched single-crystal h-BN. Phonon frequency and lifetime are measured in the 80–600 K temperature range for ^{10}B-enriched, ^{11}B-enriched and natural composition high quality crystals. Their temperature dependence is explained in the light of perturbation theory calculations of the phonon self-energy. The effects of crystal anisotropy, isotopic disorder and anharmonic phonon-decay channels are investigated in detail. The isotopic-induced changes in the phonon density of states are shown to enhance 3-phonon anharmonic decay channels in ^{10}B-enriched crystals, opening the possibility of isotope tuning of the anharmonic phonon decay processes.

PACS numbers: 78.30.-j,63.20.Ry,63.22.Np

I. INTRODUCTION

Hexagonal boron nitride (h-BN) belongs to a family of layered materials that is bound to revolutionize the field of electronic and photonic technologies in the very near future. The mechanical stacking of atomically thin layers of conducting graphene, insulating hexagonal boron nitride (h-BN) and semiconducting layered compounds such as molybdenum disulfide (MoS_2) or tungsten selenide (WSe_2) allows the creation of novel two-dimensional (2D) materials and devices with pristine interfaces bond by van der Waals forces.[1] 2D layered materials are host to a wide range of polaritonic modes that can be tailored by taking advantage of the intrinsic anisotropy of the materials and their vastly different physical properties.[2] In particular, h-BN has emerged as a promising natural hyperbolic material capable of supporting phonon-polaritons for applications in hyperlensing and sub-diffractional resonators.[3]

The issue of thermal management in electronic devices of reduced dimensionality is of paramount importance.[4] Phonon decay channels and their role in limiting ballistic transport were theoretically investigated in graphitic materials.[5] h-BN displays very high basal plane thermal conductivity that is retained down to a few monolayers[6] and may enhance lateral heat spreading when h-BN is used as dielectric support for electronic devices. Recently, ultrafast carrier cooling has been achieved in graphene–h-BN heterostructures thus overcoming the hot phonon bottleneck that limits the performance of graphene based devices.[7] Isotopic disorder in natural abundance crystals is known to scatter phonons and decrease the thermal conductivity. A thermal conductivity enhancement of $\sim$ 58% was found on isotopically pure ^{12}C graphene with respect to natural abundance graphene.[8] For h-BN, an increase in excess of 100% in the room-temperature thermal conductivity has been predicted with isotopic enrichment.[9] The absence of mass-disorder scattering in isotopically pure crystals significantly enhances the phonon lifetimes. This provides opportunities for reducing the optical losses in hyperbolic phonon-polariton devices, where the phonon-polariton modal lifetimes are on the order of the lifetimes of the optical phonons themselves.[2] Indeed, ultralow-loss polaritons have been recently reported in isotopically pure boron nitride.[10] Another area in which isotopic enrichment plays a crucial role is the development of high-efficiency solid-state neutron detectors. The ^{10}B isotope has a very large capture cross-section for thermal neutrons, and detectors based on ^{10}B enriched (99.9%) h-BN have demonstrated the highest detection efficiency (51.4%) for solid-state detectors to date.[11]

Even though a good knowledge of phonons in 2D layered materials can prove to be a powerful tool to guide the rapid development of this ever-expanding research area, some aspects of lattice dynamics of h-BN are still source of debate.[12] Whereas phonon anharmonicities have been thoroughly studied both from first principle calculations[5] and by optical spectroscopy[13] in graphitic materials, only recently has the phonon anharmonicity been addressed in h-BN.[14] Very recently, a modification of the electron density distribution in isotopically enriched ^{10}BN leading to an isotopic tuning of the van der Waals interactions has been reported.[15] This work highlights the importance of the electron-phonon interaction in determining the properties of isotope-engineered layered crystals. To date, experimental systematic studies of the effect of isotopic substitution on the lattice dynamics of layered crystals are lacking. We address this topic in isotopically-purified h-BN.

Phonon lifetimes are customarily measured in the frequency domain by means of high-resolution Raman scattering experiments,[16] in which the Raman line width Γ_R is related to the phonon lifetime τ through the energy-time Heisenberg uncertainty principle ($\tau^{-1} = 2\pi c \Gamma_R$). Furthermore, the temperature dependence of the Raman line shape carries a wealth of information on the phonon decay processes which limit the phonon lifetime and govern the buildup of hot phonon populations.[14,17] In this work, we present a Raman scattering study of the temperature dependence of the high-frequency *in-plane* Raman active mode (E_{2g} symmetry) on isotopically enriched h-BN single crystals. A detailed analysis of the results underlines the importance of the strongly anisotropic character of the laminar van der Waals crystals and reveals subtle isotopic effects in the phonon decay channels for the high-energy E_{2g} phonon of h-BN.

II. CRYSTAL STRUCTURE AND ANISOTROPY

The structure of h-BN is similar to that of isoelectronic graphite and it consists of layers of flat B_3N_3 hexagons separated by an interplanar distance $\frac{1}{2}c$. However, while graphite has non-polar C–C intralayer bonds, h-BN exhibits highly polar B–N bonds, which lends h-BN its electrical insulating character and results in an effective charge buildup at the B and N sites. Although the long-range electrostatic potential due to partially charged centers falls off very rapidly with the distance from the h-BN layer and has therefore a negligible effect on the interlayer distance, the minimization of the residual electrostatic potential favors the AA' stacking in which a partially negatively charged N atom in one layer is located on top of a partially positively charged

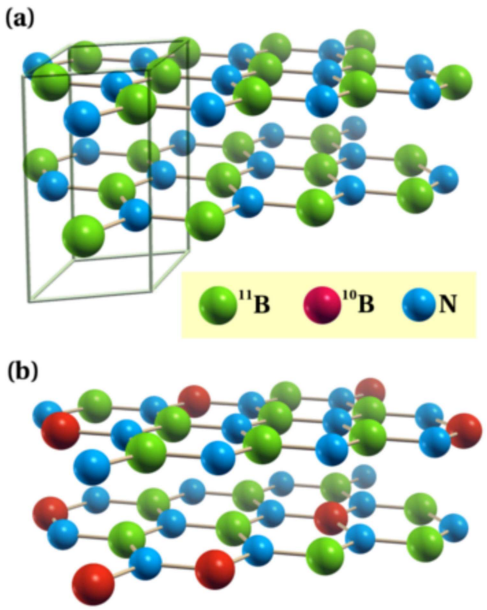

FIG. 1. Perspective view of a honeycomb bilayer conforming the crystalline structure of *h*-BN. The crystalline structure of *h*-BN consists of layers of flat, covalently bonded B_3N_3 hexagons anchored together by weak van der Waals forces. (a) Isotopically pure crystal. The primitive cell of the *h*-BN Bravais lattice containing two formula units is shown. (b) Natural isotopic composition (80% ^{11}B / 20% ^{10}B) crystal with a random distribution of ^{10}B atoms at the cation sites.

B atom of the adjacent layer (see Fig. 1). On the other hand, the interlayer distance is primarily determined by the van der Waals forces.[18] The weak interlayer forces compared to the strong polar B–N bonds result in a highly anisotropic structure. This character manifests itself in a strongly anisotropic thermal expansion with an anomalous negative coefficient in the basal plane which is related to the intrinsic bending instability coupled to the *in-plane* stretching modes of the isolated layers.[19] The thermal expansion coefficient along the *c* axis is positive and, owing to the weak interlayer forces, typically one order of magnitude higher than in the basal plane. The strong crystal anisotropy is also reflected in the phonon modes, which can be classified into modes with atomic displacements in the basal plane and modes with atomic displacements along the *c* axis, the latter typically displaying lower frequencies because of the weaker interlayer interaction.

III. METHODS AND THEORY

The study of phonon anharmonicity was carried out by means of Raman scattering on isotopically enriched as well as on natural isotopic composition *h*-BN single crystals.

A. Sample growth

The isotopically enriched samples were grown from high purity elemental ^{10}B (99.2 at%) or ^{11}B (99.4 at%) powders. A Ni-Cr-B powder mixture at 48, 48, 4 wt% respectively was loaded into an alumina crucible and placed in a furnace. The *h*-BN with the natural distribution of boron isotopes was made with 50 wt% Ni and 50 wt% Cr mixtures with a hot-pressed ceramic *h*-BN crucible, which also served as the source material. The furnace was evacuated and then filled with N_2 and forming gas (5% hydrogen in balance argon) to a constant pressure of 850 Torr. During the reaction process, the N_2 and forming gases continuously flowed through the system with rates of 125 sccm and 25 sccm, respectively. With the pure boron sources, all the nitrogen in the *h*-BN crystal originated from the flowing N_2 gas. The forming gas was used to minimize oxygen and carbon impurities in the *h*-BN crystal. After a dwell time of 24 hours at 1550 °C, the *h*-BN crystals were precipitated by cooling at a rate of 1 °C/h to 1500°C, and then the system was quickly quenched to room temperature.

B. Raman scattering measurements

The Raman scattering measurements were carried out in backscattering configuration from the *c* face using the 514.5 nm line of an Ar^+ laser. The scattered light was analyzed using a Jobin-Yvon T64000 triple spectrometer equipped with a LN_2-cooled charge-coupled device (CCD) detector. The Raman spectra were obtained in the triple-additive configuration of the spectrometer with 100 μm slits, which corresponds to a spectral bandwidth of ~ 0.7 cm^{-1}. Intrinsic phonon line widths were obtained by taking into account signal convolution with the Gaussian response function of the spectrometer. The spectra were calibrated using the 546.075 nm line of a Hg lamp. A TBT-AirLiquide LN_2 cryostat equipped with a platinum resistance sensor and a temperature controller was employed for the low-temperature measurements up to room temperature. The sample was mounted on a copper disk with a central 500 μm diameter hole. The small *h*-BN platelet was glued with silver lacquer around the hole rim to ensure good thermal

contact, while the central part remained clear so that the background signal from the silver lacquer was minimized. For the high temperature measurements, a Linkam THMS600 heating stage was used. The sample was mounted on an in-house-made sample holder consisting of a thin copper disk with a central pillar and a 500μm diameter hole. A thin coating of conductive silver silicon grease around the hole and between the copper disk and the THMS600 heating block was applied to ensure good thermal contact. The temperature was monitored by a thermocouple attached to the central pillar close to the sample location. The sample space was purged with nitrogen gas. The laser power on the sample was kept very low (8 mW in the macrocamera setup and 700 μW in the micro-Raman setup) to avoid heating effects.

C. Density functional theory calculations

Ab initio calculations based on density functional theory (DFT) constitute the standard, most accurate theoretical description of the lattice dynamics. Layered structures pose significant challenges to common approaches to DFT such as the local density approximation (LDA) or the generalized gradient approximation (GGA), as the long-range, non-local correlated charge fluctuations are not considered in the exchange and correlation energy.[20] Indeed, the GGA dramatically fails for h-BN as it gives no binding between the layers.[20] However, the LDA yields a fortuitous good description of the structural energy of graphite and h-BN.[21] LDA has previously been applied to calculate the phonon dispersion in h-BN with excellent results.[12,14] Therefore, we employ here DFT calculations in the LDA approximation using Troulliers-Martins pseudopotentials in the Teter-Pade approximation as implemented in the ABINIT code.[22] A $9\times9\times9$ Monkhorst-Pack grid was used for integration over the Brillouin zone with an energy cutoff of 70 hartree. Phonon frequencies were obtained using a perturbation-theory linear-response approach on a mesh of k points and interpolated to arbitrary wave vectors for the calculation of phonon dispersion and phonon density of states.

1. *Temperature effects: quasiharmonic approximation*

Temperature effects are not taken into account in standard DFT calculations, which model the system implicitly at zero temperature. In a harmonic crystal the restoring force depends on the departure from the equilibrium position, not on the equilibrium position itself, and

therefore the dependence of the free energy on lattice parameters is totally contained in the ground state total energy. However, if the dependence of the phonon frequencies on the lattice parameters is introduced (quasiharmonic approximation), the equilibrium lattice parameters obtained from the minimization of the Helmholtz free energy do depend on temperature and the crystal exhibits a finite thermal lattice expansion. In the quasiharmonic approximation, in addition to a purely structural contribution which depends only on the strains associated with the lattice parameters a and c, the Helmholtz free energy contains a temperature-dependent contribution due to phonons that can be modeled by a canonical ensemble of harmonic oscillators (see Appendix A).

Thermal lattice expansion induces temperature-dependent phonon-frequency shifts which must be taken into account for a correct analysis of phonon anharmonicity. The evaluation of these shifts is particularly complex in layered compounds because of the strong anisotropy and the anomalous *in-plane* thermal expansion. The approach we follow in this work is to use Eqs. (A6) and (A7) to evaluate the change in lattice parameters with temperature, and then DFT calculations are performed to determine the phonon frequencies for the new lattice parameters at a given temperature. The summations in Eqs. (A6) and (A7) are evaluated using the set of 12 special reciprocal-space points derived by Chadi and Cohen.[23]

D. Perturbation theory of isotopic and anharmonic phonon effects

Small departures from the harmonic lattice Hamiltonian give rise to coupling of the harmonic eigenstates that result in shifts and broadenings of the phonon lines. These can be described in the perturbation theory framework by a phonon renormalization given by the complex phonon self-energy $\Pi(\omega) = \Delta(\omega) + i\Gamma(\omega)$ (see Appendix B).[16] The real and imaginary parts of the self-energy correspond, respectively, to the frequency shift and broadening of the phonon line, and they are related by a Kramers-Kronig transformation.

1. *Isotopic-disorder-induced phonon renormalization*

Whereas ^{14}N makes up most of the naturally occurring nitrogen (99.63%) and can therefore be considered isotopically pure, natural boron is made up of two stable isotopes, ^{10}B and ^{11}B with relative abundances of 19.9% and 80.1%, respectively. Given the relatively low mass of

boron, its natural isotopic distribution in h-BN introduces significant mass fluctuations in the B sublattice. The degree of mass fluctuation in the sublattice can be measured in terms of the mass variance $g = \sum_i C_i[1-(M_i/\langle M\rangle)]^2$, where M_i is the isotope mass, C_i its relative abundance, and $\langle M\rangle$ is the average mass. For the case of BN, $g = 1.354\times10^{-3}$. This value is nearly one order of magnitude higher than the Ga mass variance in natural GaAs, and therefore strong isotopic-disorder effects should be expected in h-BN.

Isotopic-disorder effects were evaluated in the $^{\mathrm{Nat}}$BN sample assuming a random distribution of the ^{10}B atoms in the boron sublattice. The scattering rate, which is twice the imaginary part of the phonon self-energy, was obtained from Eq. (C2) using the phonon eigenvectors determined by the ABINIT code. The phonon shift, which corresponds to the real part of the phonon self-energy was calculated through a Kramers-Kronig transformation.

2. *Anharmonic phonon renormalization*

The finite lifetime of the phonons as they decay into phonons in other branches through decay processes that conserve energy and crystal momentum give rise to a temperature dependent broadening of the Raman line. A purely real additional contribution to the phonon self-energy [see Eq.(B3)] arises from phonon scattering with pairs of opposite wave-vector phonons.[14,24] This contribution is particularly relevant in layered crystals, where the weak interlayer interactions give rise to very low energy modes whose population increases rapidly with temperature and significantly contribute to the phonon scattering mechanism.[14]

To analyze our Raman data, we follow a semiempirical approach in which the full width at half maximum (FWHM) of the phonon line is evaluated over a range of temperatures from DFT calculations as described in Appendix B. The FWHM temperature dependence is then fitted to the experimental values obtained from the Raman spectra using the anharmonic effective potentials as free parameters. Once the anharmonic effective potentials are determined, the anharmonic-decay induced frequency shift is calculated from a Kramers-Kronig transformation of the imaginary part of the self-energy. Finally, the frequency shift associated with phonon scattering is added and the effective potential for phonon scattering is determined by fitting to the temperature dependence of the phonon frequency measured in the Raman experiments.

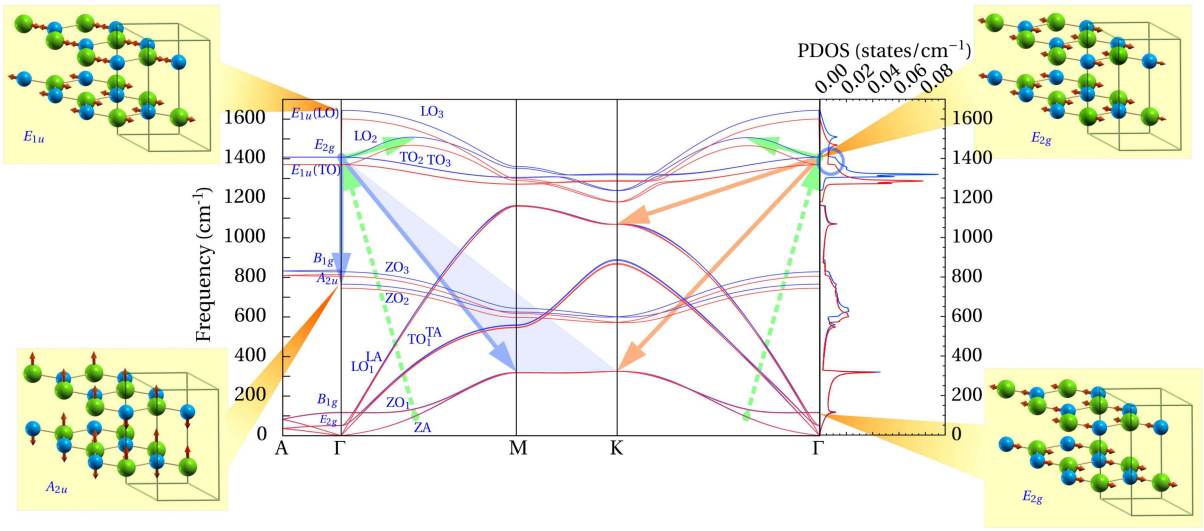

FIG. 2. Phonon dispersion along the main symmetry lines and the corresponding phonon density of states for isotopically pure ^{10}BN (blue lines) and ^{11}BN (red lines). Encircled is the step-like ridge in the phonon density of states around the frequency of the high-energy E_{2g} mode. The main phonon decay channels (see text) are indicated by arrows. The atomic motions of the E_{2g} Raman-active modes as well as those of the infrared active modes (E_{1u} and A_{2u}) are illustrated.

IV. RESULTS AND DISCUSSION

Figure 2 displays the phonon dispersion and the corresponding phonon density of states calculated for isotopically pure ^{10}BN and ^{11}BN (blue and red lines, respectively). The high-energy *in-plane* optical modes exhibit a significant frequency shift (~ 35 cm^{-1}) over the whole Brillouin zone, whereas the isotopic shift is reduced for the mid-energy *c*-polarized optical modes and virtually inexistent for the low-energy acoustic modes. We focus our isotopic study on the Raman-active, high-energy E_{2g}^{high} mode. For this mode, the B and N atoms vibrate against each other in the hexagonal plane, as sketched in Fig. 2. On account of their similar atomic masses, the amplitude of B and N vibrations do not differ significantly. Unlike GaN, where the high-energy *in-plane* E_2 mode is dominated by the vibration of the lighter N atom and the low-energy E_2 mode mostly involves the motion of the heavier Ga atom,[25] in *h*-BN the high-energy character is conferred to the E_{2g}^{high} mode by the antiparallel motion of the B and N atoms probing the stronger *in-plane* covalent bonding. In contrast, in the low-energy E_{2g} mode the B and N atoms in each layer vibrate in phase giving rise to a low-energy interlayer shear mode (see

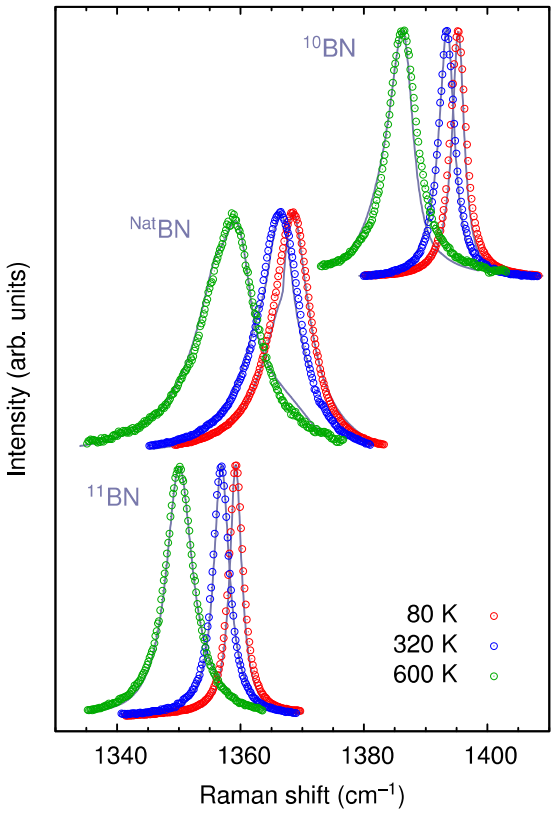

FIG. 3. Raman spectra of ^{10}BN, natural-composition BN, and ^{11}BN single crystals recorded at 80 K, 320 K, and 600 K in backscattering configuration from a *c* face. Solid lines correspond to line-shape model fits to the data.

Fig. 2). The E_{2g}^{low} can be viewed as a zone folding of the *in-plane* acoustic branches along the *A* direction arising from the alternate layout of B and N atoms along the *c* direction. On the other hand, the E_{2g}^{high} mode is an archetypal vibrational mode whose frequency should scale as the inverse square-root of the reduced mass and is best suited for the study of isotopic effects.

A. Raman spectra of the E_{2g}^{high} mode: variation with isotopic composition

Figure 3 shows Raman spectra (empty circles) of ^{10}BN, natural-composition BN, and ^{11}BN single crystals at different temperatures. The solid gray lines are line-shape model fits to the spectra that will be explained below. At 80 K, the E_{2g}^{high} frequency decreases from 1395 cm^{-1} for the ^{10}BN sample to 1359 cm^{-1} for the ^{11}BN sample. The ratio of E_{2g}^{high} frequencies is commensurate with the inverse square-root of their respective reduced masses. In both cases the

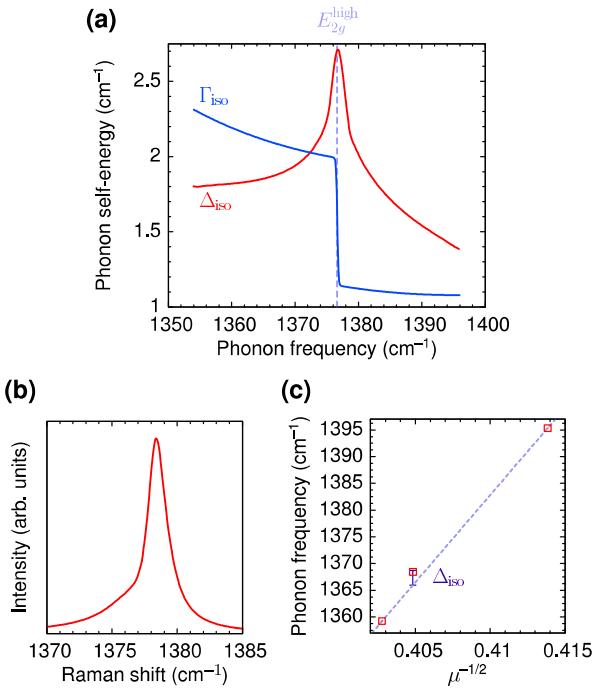

FIG. 4. (a) Real (Δ_{iso}, red line) and imaginary (Γ_{iso}, blue line) parts of the isotopic-disorder-induced phonon self-energy around the E_{2g}^{high} frequency. (b) Asymmetric broadening of the E_{2g}^{high} line produced by the isotopic-disorder-induced scattering. (c) Measured E_{2g}^{high} phonon frequencies at 80 K (red squares) as a function of the inverse square-root of the effective mass. The linear dependence predicted by the virtual-crystal-approximation is depicted by a dashed line. The vertical segment indicates the real part of the phonon self-energy which yields the isotopic-disorder-induced phonon shift.

Raman line is a narrow and perfectly symmetrical Lorentzian line, with a FWHM of 2.7 cm^{-1} at 80 K, indicating the high crystalline quality of the samples. In contrast, the E_{2g}^{high} peak of the natural isotopic composition sample is much broader (FWHM of 7.2 cm^{-1} at 80 K) and visibly asymmetric. With increasing temperature, similar frequency downshifts and broadenings of the E_{2g}^{high} mode occur for all isotopic compositions, and the symmetrical Lorentzian line shape is maintained in the isotopically pure samples.

1. *Mass-disorder effects*

In the *h*-BN crystal with natural abundance of boron isotopes, the mass fluctuations in the boron sublattice break the translational symmetry, and crystal momentum conservation is relaxed. This allows elastic scattering of phonons, leading to a phonon self-energy renormaliza-

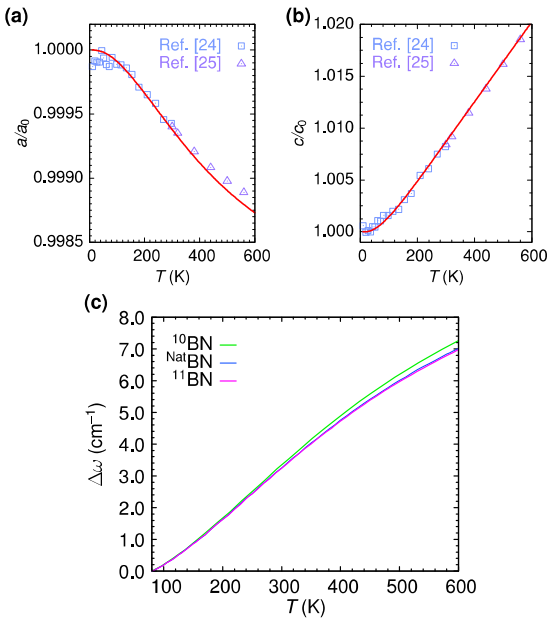

FIG. 5. (a) Temperature dependence of the a lattice parameter obtained by DFT calculations in the quasi-harmonic approximation for the ^{Nat}BN crystal. (b) Idem, for the c lattice parameter. (c) Contribution of the lattice expansion to the thermal shift of the E_{2g}^{high} mode relative to the frequency at 80 K.

tion as described in Appendix C. The real and imaginary parts of the phonon self-energy, which determine the frequency shift and broadening of the phonons, are plotted in Fig. 4 (a) for the natural isotopic composition h-BN around the E_{2g}^{high} frequency.

The imaginary part of the phonon self-energy displays a steep edge at the E_{2g}^{high} frequency which is related to the prominent step-like structure that can be seen at the E_{2g}^{high} frequency in the phonon density of states (see encircled area in Fig. 2). Since the isotopic-disorder-induced scattering rate is increasingly higher for frequencies just below the E_{2g}^{high} frequency, it leads to an asymmetric line shape with a low-energy tail. This is illustrated in Fig. 4(b), where the broadened E_{2g}^{high} line due solely to the isotopic-disorder-induced phonon self-energy is plotted. Similar asymmetric line shapes associated with ridge-like structures in the phonon density of states have been reported in other semiconductors.[26–29]

The real part of the phonon self-energy, obtained from the Kramers-Kronig transformation of the scattering rate, displays a peak at the E_{2g}^{high} frequency. As can be seen in Fig. 4(c), the magnitude of the real part of the phonon self-energy nicely reproduces the departure of the E_{2g}^{high} frequency in ^{Nat}BN from the virtual-crystal-approximation prediction of a linear dependence on the inverse square-root of the effective mass.

2. Thermal lattice expansion

Regarding the temperature dependence of the E_{2g}^{high} frequency, an obvious source of phonon shift is the thermal expansion of the lattice. The variation of the lattice parameters with temperature is obtained by integration of the lattice expansion coefficients [Eqs. (A6) and (A7)] derived in the quasi-harmonic approximation (see Sec. III C 1 and Appendix A). Then, the phonon frequencies for the temperature-dependent lattice parameters can be evaluated for the thermally strained lattice. Although LDA calculations tend to overbind and yield a and c parameter values slightly lower (by 0.4% and 2%, respectively) than the experimental values reported in Ref. 30 and 31, the quasi-harmonic approximation yields a temperature dependence of the lattice parameter in excellent agreement with experiment. Figures 5(a) and (b) show the thermal expansion of the a and c parameters relative to their values at zero temperature, compared to experimental values available in the literature. Since the phonon spectrum changes upon isotopic substitution (see Fig. 2), the vibrational contribution to the Helmholtz [Eq. (A2)] energy will also change. Therefore, differences in the thermal expansion behavior are to be expected among the different isotopical compositions. Nevertheless, the effect turns out to be quite small and it only amounts to ~ 0.3 cm^{-1} at 600 K between the ^{10}BN and ^{11}BN crystals, which is negligible compared with the substantial thermal expansion blueshift of the E_{2g}^{high} frequency over the temperature range studied [see Fig. 5 (c)].

In the Raman experiments (see Fig. 3), the E_{2g}^{high} frequency decreases as the temperature increases, contrary to the behavior one would expect from the negative *in-plane* thermal expansion coefficient. Therefore, phonon anharmonicity must play a salient role in shaping up the temperature dependence of this phonon mode.

B. Phonon anharmonic decay channels: sensitivity to isotopic composition

Phonon anharmonic decay processes limit the phonon lifetime and yield line broadenings that can be evaluated in perturbation theory as outlined in Appendix B. The line broadenings resulting from anharmonic phonon decay are essentially proportional to the combined two-phonon density of states and the most likely channels for phonon decay can be identified on the phonon dispersion (Fig. 2) as pathways that conserve energy and momentum. As can be seen in Fig. 2, the acoustic branches change very little with isotopic substitution, whereas the

largest isotopic shifts take place in the higher energy modes of E_{2g} and E_{1u} symmetry. This is related to the higher real space displacement of the lighter cation in these modes. For instance, in the E_{2g}^{high} and E_{1u} eigenvectors, the ratio between B and N displacements is ~ 1.3, whereas in the E_{2g}^{low} eigenvectors the magnitude of the B and N displacements is virtually the same.

The different response of acoustic and mid- and high-frequency optical modes to isotopic substitution and the corresponding shift of the phonon density of states revealed in Fig. 2 have a bearing on the relative efficiency of the anharmonic decay channels. As an example of this, consider the most likely decay channel into two lower energy phonons (depicted by the orange arrows in Fig. 2)

$$E_{2g}^{\text{high}}(\Gamma) \rightarrow \left\{ \begin{array}{c} \text{LA} \\ \text{LO}_1 \end{array} \right\}(K) + \left\{ \begin{array}{c} \text{ZO}_1 \\ \text{ZA} \end{array} \right\}(K). \tag{1}$$

This is a relatively minor contribution in the case of $^{\text{Nat}}$BN because of the slight frequency mismatch with the sum of frequencies of the phonon decay products, which is somewhat higher than the actual E_{2g}^{high} frequency. Since the phonon decay products belong to the acoustic or acoustic-like branches which are practically unaffected by isotopic substitution, their sum is unaltered in the ^{10}BN crystal whereas its E_{2g}^{high} frequency increases. This reduces the frequency mismatch and notably enhances the contribution of this decay channel to phonon anharmonic decay in ^{10}BN. On the other hand, for the phonon difference channel involving the LO_2 and ZA branches (dashed green lines in Fig. 2) a perfect match can be achieved in all cases by selecting the appropriate wave-vector along the $\Gamma - M$ or $\Gamma - K$ lines, of course at a cost of reducing the density of final phonon states.

The quartic anharmonicity channel involving the decay into a zone center phonon and a pair of opposite wave-vector phonons (depicted by the blue arrows and shaded area in Fig. 2):

$$E_{2g}^{\text{high}}(\Gamma) \rightarrow A_{2u}(\Gamma) + \left\{ \begin{array}{c} \text{ZA} \\ \text{ZO}_1 \end{array} \right\}(\text{M}-\text{K}) + \left\{ \begin{array}{c} \text{ZA} \\ \text{ZO}_1 \end{array} \right\}(\text{M}-\text{K}) \tag{2}$$

was shown to have a prominent role in the phonon decay in natural composition h-BN that could explain the observed superlinear increase of the Raman line width with temperature.[14] As a first approximation, one can consider that the dependence of the line width on temperature is primarily governed by the Bose-Einstein occupation factors. From the temperature dependence of the occupation factors, a quasi-linear increase of the FWHM should be expected from

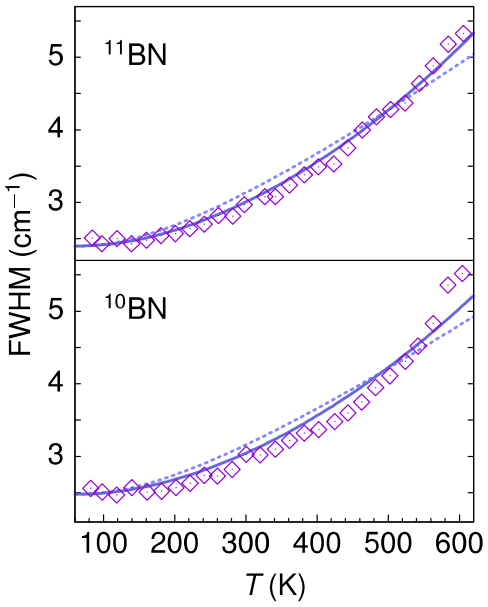

FIG. 6. (a) Temperature dependence of the FWHM of the E_{2g}^{high} Raman peak (open diamonds) for the ^{10}BN and ^{11}BN samples. The dotted lines are fits of the Bose-Einstein occupation factors corresponding to 3-phonon decay processes. The solid line includes also the Bose-Einstein occupation factors associated with the 4-phonon decay contribution defined by Eq. (2).

the lowest-order cubic anharmonicity terms. Figure 6 compares the temperature dependence of the E_{2g}^{high} line width determined from the Raman measurements on ^{10}BN and ^{11}BN samples (diamonds) with fits of the Bose-Einstein occupation factors associated with cubic anharmonic decay (dotted lines). The bowing trend displayed by the experimental points clearly deviates from the quasi-linear behavior given by the lowest-order anharmonicity. A better agreement is found when the Bose-Einsten occupation factors corresponding to the dominant 4-phonon decay process are included (solid lines). While this is only a crude approximation to the effects of anharmonic decay on the Raman line width, it clearly suggests a substantial contribution of higher-order decay channels in the case of *h*-BN. The semi-empirical model outlined in Appendix B improves on the description of anharmonic decay channels by taking into account the combined phonon density of states. The latter depends on the phonon frequencies and therefore captures the effects of isotopic substitution. It should be emphasized that the semi-empirical model, which suggests a strong contribution of the quartic anharmonicity, does not allow a univocal determination of all adjustable effective potentials, as several combinations of $V_3^{+/-}$ and V_4^+ yield fits of similar quality.

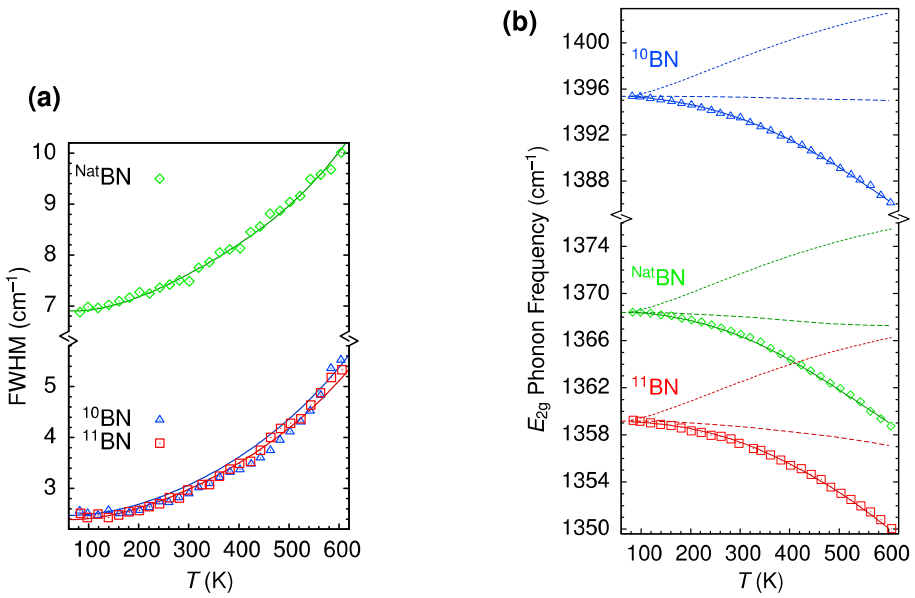

FIG. 7. (a) Temperature dependence of the FWHM of the E_{2g}^{high} Raman peak (open symbols) for the ^{10}BN, ^{11}BN and the natural composition h-BN sample. The solid lines are fits of the anharmonic phonon decay model. (b) Temperature dependence of the E_{2g}^{high} phonon frequency (open symbols) for the ^{10}BN, ^{11}BN and the natural composition h-BN sample. Solid lines are model fits to the data (see text). Dotted lines indicate the thermal expansion contribution and dashed lines correspond to the anharmonic phonon decay contribution.

In the case of $^{\text{Nat}}$BN, the temperature dependence of the FWHM could be well described by considering only the quartic term.[14] The situation is radically different in ^{10}BN following the changes in phonon frequencies introduced by the lighter cation. Isotopic substitution in ^{10}BN does not affect the frequency of the acoustic modes and increases the A_{2u} frequency in a lower degree than the E_{2g}^{high} frequency. As a consequence, the E_{2g}^{high} frequency is displaced to the high-frequency side of a steep ridge of the combined two-phonon density of states of ^{10}BN. Such steep ridge-like structures in the phonon density of states usually give rise to asymmetric Raman line shapes.[29] If only the quartic anharmonic decay channel determined by Eq. (2) were considered in the Raman line shape calculations for ^{10}BN, severely distorted asymmetric line shapes would result. This is manifestly incompatible with the narrow, symmetric Lorentzian line shapes measured in the Raman spectra of ^{10}BN shown in Fig. 3. It turns out however that, if a contribution of the 3-phonon anharmonic decay channel [Eq. (1)] is taken into account, the asymmetry is largely compensated, and physically acceptable line shapes can be gener-

TABLE I. Model parameters for the anharmonic phonon decay model used to fit the experimental data. V_3^+ and V_3^- are the effective anharmonic coupling potentials for phonon sums and differences, respectively. V_4^+ is the effective anharmonic potential for the quartic decay process. $\tilde{V}_4$ is the effective potential for the 4-phonon scattering. Γ_b is the contribution to the FWHM from residual impurities and defects other than mass defects.

sample	$\lvert V_3^+\rvert^2$ (cm^{-2})	$\lvert V_3^-\rvert^2$ (cm^{-2})	$\lvert V_4^+\rvert^2$ (cm^{-2})	$\tilde{V}_4$ (cm^{-1})	Γ_b (cm^{-1})
^{10}BN	4.0	0.5	6.9	-2.75	1.3
^{Nat}BN	4.0	0.5	9.7	-2.58	3.8
^{11}BN	4.0	0.5	10.1	-2.40	1.3

ated. As can be seen in Fig. 3, excellent model fits to the experimental Raman line shapes are obtained even at higher temperature by including explicitly the 3-phonon anharmonic decay channel in the ^{10}BN calculations. Thus, the role of the 3-phonon anharmonic decay channel is crucial to explain the Raman spectra of ^{10}BN. This enhanced role stems from the improved frequency match and combined phonon density changes that result from ^{10}B isotopic substitution as discussed above. Although the alterations in the electron density distribution reported in ^{10}BN (Ref. 15) could have some minor effect on the anharmonic potentials $V_3^{+/-}$, which are basically related to the third order derivatives of the total energy with respect atomic displacements, these are not expected to change significantly from ^{10}BN to ^{11}BN. Then, the $V_3^{+/-}$ values estimated for ^{10}BN may be extrapolated to ^{11}BN and natural compositon BN. In the latter, however, the effects of the 3-phonon decay channel are less important because of the reduction in the combined phonon density of states associated with the phonon energy mismatch.

C. Temperature dependence of the E_{2g}^{high} line width

Information about the anharmonic phonon decay channels is basically contained in the temperature dependence of the phonon line width. Figure 7(a) shows the temperature dependence of the FWHM of the E_{2g}^{high} Raman peak and the fit of the anharmonic phonon decay theory [Eqs. (B1) and (B2)] using the effective anharmonic potentials as free parameters. The

values of the parameters used for the fit are listed in Table I. The increase of the E_{2g}^{high} FWHM with temperature is very similar for all three studied samples. For both isotopically pure crystals a very low background impurity contribution ($\Gamma_b \sim 1.3$ cm^{-1}) is found, indicating the high crystalline quality of the samples. The residual impurity background is higher in the natural composition sample ($\Gamma_b \sim 3.8$ cm^{-1}).

Note that a higher value of 6.1 cm^{-1} was reported in Ref. 14 for the natural composition h-BN. This is to be expected, as in Ref. 14 no account was specifically made for scattering by mass fluctuation, and the isotopic disorder effects were generically incorporated into the background impurity scattering. The reduced value found in our present analysis, which specifically accounts for isotopic disorder, corresponds with the magnitude of the imaginary part of the phonon self-energy reported in Fig. 4(a). However, the residual impurity background is still significantly higher than the values obtained in isotopically pure samples. This might suggest that the isotopic-disorder scattering rate is actually higher than the estimates that were obtained from the perturbation theory analysis, possibly because of departure from true randomness of the actual isotope distribution. Nonetheless, the isotopic-disorder-induced broadening and the associated frequency shift are related by a Kramers-Kronig transformation, and the frequency shift thus obtained is in excellent agreement with the observed frequency shift [see Fig. 4 (c)]. Therefore, most probably the sizably larger value of Γ_b obtained for the natural composition h-BN sample truly reflects a higher concentration of point defects in the isotopically disordered lattice. This is presumably related to the use of a commercial h-BN ceramic crucible for the growth of the natural composition sample, which resulted in a less clean h-BN sample.

The value of the V_4^+ parameter, which accounts for higher order anharmonic interactions not included in the cubic anharmonicity term, is similar for ^{11}BN and natural composition samples but a slightly lower value is found for ^{10}BN. Since the isotopic change of phonon energies favors the 3-phonon decay channels in ^{10}BN and the same cubic anharmonic potentials have been used for all isotopic samples, a higher value of the V_4^+ in ^{11}BN and natural composition samples is required to compensate the lower efficiency of the 3-phonon decay processes. It should be stressed that $V_3^{+/-}$ and V_4^+ are semi-empirical model parameters that describe the temperature dependence of the Raman spectra and, while they are related to the actual anharmonic potentials (third- and fourth-order derivatives of the total energy), their values should not be literally taken as a precise determination of the anharmonic potentials.

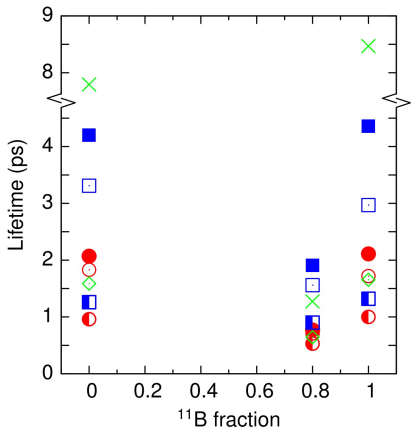

FIG. 8. E_{2g}^{high} phonon lifetimes at 80 K (filled symbols), room temperature (empty symbols), and 600 K (half-filled symbols) for isotopically pure and natural composition samples. The red circles correspond to the full phonon lifetime as obtained from the Raman line width and the blue squares indicate the intrinsic phonon lifetime associated with anharmonicity and mass-disorder effects. Green diamonds and green crosses are, respectively, experimental lifetime values and density functional theory estimates reported in Ref.[10].

In summary, the analysis of the temperature dependence of the Raman spectra of ^{10}BN reveals an enhanced effect of the 3-phonon anharmonic decay on the Raman line shape on account of the changes in phonon frequencies and density of states introduced by isotopic substitution. This allows an estimation of the strength of the third-order effective potentials which gives a consistent description of phonon anharmonic decay in isotopically enriched samples.

D. Phonon lifetime

An estimation of the phonon lifetime τ can be obtained from the Raman spectra using the energy-time uncertainty relation as

$$\Gamma_R = \frac{\hbar}{\tau} = \hbar\left(\frac{1}{\tau_i} + \frac{1}{\tau_b}\right), \tag{3}$$

where Γ_R is the FWHM (in cm^{-1}) of the Raman peak, τ_i is the intrinsic phonon lifetime associated with anharmonic decay and mass disorder, τ_b is the inverse scattering rate associated with background impurities, and $\hbar = 5.30885 \times 10^{-12}$ cm^{-1}s is Planck's constant. Lifetime values (τ) obtained from the Raman line widths after correction for the spectrometer bandwidth are displayed as red circles in Fig. 8 for three different temperatures. The intrinsic phonon life-

times τ_i are indicated by blue squares. At 80 K the phonon lifetime τ in the isotopically pure crystals is slightly above 2 ps, ~ 2.7 times higher than in natural composition samples. As already discussed, this reflects the suppression of the mass-disorder scattering and the superior crystalline quality of these samples. The intrinsic phonon lifetime τ_i is as high as ~ 4.2 ps in the isotopically pure samples, strongly suggesting that higher phonon lifetimes would be in principle feasible if better crystalline quality material with reduced background impurity could be achieved. The growth of high-quality isotopically pure *h*-BN could thus be a viable route to address the fundamental issue of optical losses in hyperbolic phonon-polariton applications and sub-diffraction imaging. While the phonon lifetime values we find at room temperature are only slightly higher than those reported in Ref. 10, our estimations of the intrinsic phonon lifetime τ_i for isotopically pure *h*-BN are roughly a factor of two lower than the *ab initio* theoretical prediction given in Ref. 10 (See Fig. 8). Thus, the expectations of achieving substantial polariton propagation lengths by reducing background impurity concentration in *h*-BN, where group velocity at which the polariton propagates can be exceptionally slow, appear to be more limited than previously suggested.[10] With increasing temperature, the phonon lifetime decreases and the differences between the intrinsic phonon lifetime and the full phonon lifetime as well as the differences between isotopically pure and natural composition samples are reduced.

E. Temperature dependence of the E_{2g}^{high} frequency: the role of 4-phonon scattering

The anharmonic frequency shift associated with the observed temperature dependence of the FWHM discussed in Sec. IV C is obtained by a Kramers-Kronig transformation of the imaginary part of the anharmonic phonon self-energy. It turns out to be rather small and insufficient to reverse the increase of E_{2g}^{high} frequency due to the *in-plane* negative thermal expansion. Both contributions are plotted for the samples with different isotopic compositions in Fig. 7(b). The anharmonic contribution (dashed line) is particularly smaller for ^{10}BN on account of the more important role that 3-phonon anharmonic decay processes play in the decay pathways compared to ^{11}BN and natural composition *h*-BN, as inferred from the FWHM analysis presented in Sec. IV C.

Thus, the large E_{2g}^{high} frequency decrease with temperature measured in all samples can only be explained by considering a 4-phonon scattering anharmonic interaction, which yields a further frequency shift that can be approximated by Eq. (B3). The effective anharmonic poten-

tial $\tilde{V}_4$ turns out to be negative because of the negative anharmonic coupling to the low-lying E_{2g}^{low} interlayer shear mode.[14] By fitting Eq. (B3) we obtain similar $\tilde{V}_4$ values for all samples (see Table I) and an excellent agreement with the experimental temperature dependence data presented in Fig. 7(b). Comparable values of $\tilde{V}_4$ are to be expected for all isotopic compositions because they are primarily determined by coupling to the low-lying modes typical of layered crystals, and the frequency of these modes remains nearly unaltered upon isotopic substitution.

By taking into account all the relevant anharmonic effects as well as the effects of isotopic disorder, a comprehensive understanding of the E_{2g}^{high} phonon in ^{10}BN, ^{11}BN and natural h-BN is achieved. The model not only describes accurately the temperature dependence of the frequency and FWHM of the E_{2g}^{high} mode, but also the line-shape alterations observed for different isotopical compositions and temperatures. As can be seen in Fig. 3, the theoretical line-shape model that takes into account all contributions yields remarkably good fits to the experimental Raman spectra.

V. CONCLUSIONS

An in-depth analysis of the E_{2g}^{high} phonon dependence on boron isotopic substitution and temperature has been presented and the interplay between the different effects that determine the E_{2g}^{high} frequency and line width has been elucidated by detailed modeling.

Isotopic-disorder-induced elastic scattering accounts for the significantly higher E_{2g}^{high} line width in natural composition h-BN compared with isotopically pure samples. A substantial increase in phonon lifetime by nearly a factor of 3 is observed in isotopically pure samples. Our data suggests that further increase in lifetime should be possible if background impurity concentration could be reduced. Whereas for the isotopically pure samples the E_{2g}^{high} frequency scales with the inverse square-root of the reduced mass, for the natural composition sample it shows a departure from the linear dependence on reduced mass. Both the sign and the magnitude of such a departure are accurately predicted by our perturbation theory model of isotopic mass-disorder effects.

The effect of the anomalous *in-plane* negative thermal expansion of the laminar h-BN crystal has been carefully studied in the quasi-harmonic approximation. While the isotopic substitution effect on the thermal shift of the E_{2g}^{high} frequency is negligible, thermal expansion pro-

duces a sizable blueshift of the E_{2g}^{high} mode with temperature. This is in stark contrast with the experimental frequency downshift of the E_{2g}^{high} Raman peak with increasing temperature. The latter is explained by the dominant contribution of the 4-phonon scattering anharmonic interaction, which is found to be of similar strength for all isotopic compositions.

The impact of isotopic substitution on the anharmonic decay channels has been investigated. DFT calculations reveal that ^{10}B isotopic substitution in h-BN yields an upward shift of the phonon bands which is most marked in the high energy optical modes, whereas the acoustic modes show very little sensitivity to isotopic substitution throughout the Brillouin zone. The uneven shift of the phonon bands has implications on the phonon anharmonic decay channels, which for ^{10}BN include a relevant decay path into two phonons that has a more prominent role than in ^{11}BN and natural composition BN because of its closer phonon energy match. The influence of this 3-phonon anharmonic decay channel is key to explain the symmetric Raman line shape observed in the experiments on the ^{10}BN crystal. This constitutes the first demonstration of the isotope tuning of the phonon anharmonic decay in layered compounds arising from the small sensitivity to isotopic substitution of the acoustic and shear modes. These effects in isotopically enriched h-BN open the possibility of exploring isotope substitution in other layered compounds for phonon lifetime engineering.

ACKNOWLEDGMENTS

This work has been financially supported by the Spanish MINECO/FEDER under Contract No. MAT2015-71035-R. B. G. acknowledges the Russian Megagrant program (Ioffe Institute of RAS, contract #14.W03.31.0011). Support for the h-BN crystal growth from the Materials Engineering and Processing program of the National Science Foundation, award number CMMI 1538127 is greatly appreciated.

Appendix A: Thermal expansion in the quasi-harmonic approximation

In the quasi-harmonic approximation, the Helmholtz free energy of a h-BN crystal with lattice parameters $\{a_i\} = a, c$ contains a contribution from the elastic energy associated with the strain field produced by the thermal expansion and a temperature-dependent contribution due

to phonons:

$$F(\{a_i\},T) = E(0,0) + \frac{1}{2}V_0 K_{ij}\epsilon_i\epsilon_j + F_{\text{vib}}(\{a_i\},T). \tag{A1}$$

Here, $E(0,0)$ is the ground state total energy at zero temperature, K_{ij} is the elastic modulus tensor, and $\epsilon_i = (a_i - a_i^0)/a_i^0$ is the elastic strain at temperature T.

The phonon contribution to the Helmholtz free energy corresponding to a canonical ensemble of harmonic oscillators is given by[32]

$$\begin{aligned} F_{\text{vib}}(\{a_i\},T) = &\frac{1}{2}\sum_{\mathbf{q},j}\hbar\omega_{\mathbf{q},j}(\{a_i\}) \\ &+ k_B T\sum_{\mathbf{q},j}\ln\left[1-\exp\left(-\frac{\hbar\omega_{\mathbf{q},j}(\{a_i\})}{k_B T}\right)\right], \end{aligned} \tag{A2}$$

where k_B is the Boltzmann constant, $\hbar$ is the Plank constant, $\omega_{\mathbf{q},j}$ is the phonon frequency, and the sum is over all phonon wave vectors $\mathbf{q}$ and all phonon branches j.

The equilibrium lattice parameters at any temperature can be obtained by minimization of the Helmholtz free energy:

$$\frac{\partial F}{\partial \epsilon_i} = V_0 K_{ij}\epsilon_j + \frac{\partial F_{\text{vib}}}{\partial \epsilon_i} = 0. \tag{A3}$$

By multiplying Eq. (A3) by the elastic compliance tensor $S_{ij} = (K^{-1})_{ij}$ we obtain

$$\epsilon_i = -\frac{1}{V_0}S_{ij}\frac{\partial F_{\text{vib}}}{\partial \epsilon_j}, \tag{A4}$$

and then the thermal expansion coefficients are given by

$$\alpha_i = \frac{\partial \epsilon_i}{\partial T}\Big|_{\sigma=0} = -\frac{S_{ij}}{V_0}\frac{\partial^2 F_{\text{vib}}}{\partial T\partial \epsilon_j}. \tag{A5}$$

Substituting Eq. (A2) into Eq. (A5), the thermal expansion coefficients in the anisotropic uniaxial crystal can be expressed as[24]

$$\begin{aligned} \alpha_a = \frac{k_B}{V_0}\sum_{\mathbf{q}j}\xi^2\text{csch}^2(\xi)[&(S_{11}+S_{12})\gamma_a(\mathbf{q},j) \\ &+ S_{13}\gamma_c(\mathbf{q},j)] \end{aligned} \tag{A6}$$

$$\alpha_c = \frac{k_B}{V_0}\sum_{\mathbf{q}j}\xi^2\text{csch}^2(\xi)[2S_{31}\gamma_a(\mathbf{q},j) + S_{33}\gamma_c(\mathbf{q},j)] \tag{A7}$$

where we have introduced the Grüneisen parameters $\gamma_{a_i}(\mathbf{q},j) = -(a_{i,0}/\omega_{\mathbf{q}j})(\partial\omega_{\mathbf{q}j}/\partial a_i)$, and $\xi = \hbar\omega_{\mathbf{q}j}/2k_B T$.

Appendix B: Perturbation theory of anharmonic decay

Perturbation theory of anharmonic phonon decay has been amply discussed in the literature and has been examined in detail for h-BN (see Ref. 14 and references therein). We give here only the most relevant expressions that will be used to analyze our data.

The renormalization of the phonon energy due to anharmonic phonon-phonon interactions is described by the complex phonon self-energy $\Pi(\mathbf{q}, j; \omega) = \Delta(\mathbf{q}, j; \omega) + i\Gamma(\mathbf{q}, j; \omega)$. To the lowest order in perturbation theory, the imaginary part of the phonon self-energy is given by

$$\Gamma(\omega) = |V_3^+|^2(1 + n_1 + n_2)\rho^+(\omega) + |V_3^-|^2(n_2 - n_1)\rho^-(\omega), \tag{B1}$$

with $\rho^+(\omega)$ and $\rho^-(\omega)$ the two-phonon sum and difference DOS, and V_3^+ and V_3^- the effective third-order anharmonic potentials for decay into phonon sums and phonon differences, respectively. n_1 and n_2 are the Bose-Einstein factors for the phonons involved in the phonon sum or phonon difference. The first term in Eq. (B1) describes the decay of a phonon into two lower frequency phonons of opposite wave vectors, and the second term corresponds to the annihilation of the phonon and the creation of a higher energy phonon. Higher-order processes involving four phonons can be approximated by the following term[17]:

$$\begin{aligned}\Gamma^{(4)}(\omega) \sim\ & |\tilde{V}_4^+|^2\{[n(\omega_1^+) + 1][n(\omega_2^+) + 1][n(\omega_3^+) + 1] \\ & - n(\omega_1^+)n(\omega_2^+)n(\omega_3^+)\}\rho^+(\omega - \omega_1^+) \\ & + |\tilde{V}_4^-|^2\{[n(\omega_1^-) + 1][n(\omega_2^-) + 1]n(\omega_3^-) \\ & - n(\omega_1^-)n(\omega_2^-)[n(\omega_3^-) + 1]\}\rho^-(\omega - \omega_1^-),\end{aligned} \tag{B2}$$

where ω_1 is the frequency of a zone-center mode and ω_2, ω_3 are the frequencies of opposite wave-vector phonon modes satisfying energy conservation.

The most likely decay channels can be readily identified by inspection of the phonon dispersion plot calculated by DFT. Then, the imaginary part of the phonon self-energy can be evaluated by means of Eqs. (B1) and (B2) using the two-phonon density of states obtained from the DFT calculations, with the effective anharmonic potentials as adjustable parameters. The real part of the phonon self-energy is obtained from a Krammers-Kronig transformation of Eqs. (B1) and (B2). A further, purely real contribution to the phonon self-energy arises from a first-order loop diagram that describes the scattering between the zone center phonon under consideration and a pair of opposite wave-vector phonons. This process yields an additional frequency

shift that can be approximated by[14]

$$\Delta^{s}(T) \approx \tilde{V}^{s} \int_{0}^{\infty} d\omega [n(\omega, T) - n(\omega, T_0)] \rho(\omega), \tag{B3}$$

where $\tilde{V}^{s}$ is an effective phonon scattering constant, $n(\omega, T)$ is the Bose-Einstein occupation factor, and $\rho(\omega)$ is the phonon density of states.

The Raman line shape of the renormalized phonon is given by

$$I(\omega) \propto \frac{\Gamma(\omega)}{[\omega_0 + \Delta_0 + \Delta(\omega) - \omega]^2 + \Gamma(\omega)^2}, \tag{B4}$$

where ω_0 is the bare phonon frequency and Δ_0 is the thermal expansion shift. Note that, in the limit of slowly varying $\Gamma(\omega)$, the FWHM of the Raman line shape corresponds to two times the imaginary part of the phonon self-energy.

Appendix C: Isotopic-disorder-induced phonon self-energy

The isotopic-disorder-induced elastic scattering causes a phonon renormalization determined by the phonon self-energy $\Pi_{iso} = \Delta_{iso} + i\Gamma_{iso}$. The imaginary part of the self-energy is related to the isotope-disorder-induced scattering rate as $(2\pi c \tau_{iso})^{-1} = 2\Gamma_{iso}$. A crystal with isotopic atoms randomly distributed on the sublattice κ is characterized by the mass variance

$$g(\kappa) = \sum_{i} C_i [1 - (M_i / \langle M \rangle)]^2, \tag{C1}$$

where M_i is the isotope mass, C_i its relative abundance, and $\langle M \rangle$ is the average mass. The scattering rate for such a crystal was calculated by S. Tamura to be[33]

$$\begin{aligned} \tau^{-1}(j\mathbf{q};\omega) = & \frac{\pi}{2N} \omega_j^2(\mathbf{q}) \sum_{j',\mathbf{q}'} \delta[\omega - \omega'_j(\mathbf{q})] \\ & \times \sum_{\kappa} g(\kappa) |\mathbf{e}^*(\kappa | j'\mathbf{q}') \cdot \mathbf{e}(\kappa | j\mathbf{q})|^2. \end{aligned} \tag{C2}$$

Here N is the number of unit cells and $\mathbf{e}(\kappa|1\,j\mathbf{q})$ is the orthonormal eigenvector of the sublattice κ of the phonon with wave vector $\mathbf{q}$ in the j branch. In crystals with cubic symmetry Eq. (C2) can be simplified by recognizing that vibrations polarized along three orthogonal directions are equivalent by symmetry. Then, the scattering rate is described by the squared amplitudes of the initial phonon multiplicated by the projected phonon density of states.[27,33] This simplified approach cannot be applied in the case of lamellar crystals because of the strong anisotropy

between *in-plane* vibrations and vibrations polarized along the *c*-axis. Therefore, the full expression Eq. (C2) must be retained to correctly describe isotopic disorder in this type of crystals.

Once the imaginary part of the phonon self-energy is obtained by evaluation of Eq. (C2) using the eigenvectors provided by the ABINIT code, the real part can be readily determined through a Kramers-Kronig transformation

$$\Delta_{\mathrm{iso}}(j\mathbf{q};\omega) = -\frac{1}{\pi}\mathscr{P}\int_0^\infty \frac{\omega'}{\omega'^2-\omega^2}[2\pi c\tau_{\mathrm{iso}}(\omega')]^{-1}d\omega'. \tag{C3}$$

---

[1] T. Roy, M. Tosun, J. S. Kang, A. B. Sachid, S. B. Desai, M. Hettick, C. C. Hu, and A. Javey, ACS Nano **8**, 6259 (2014).

[2] T. Low, A. Chaves, J. D. Caldwell, A. Kumar, N. X. Fang, P. Avouris, T. F. Heinz, F. Guinea, L. Martin-Moreno, and F. Koppens, Nat. Mater. **16**, 182 (2016).

[3] P. Li, M. Lewin, A. V. Kretinin, J. D. Caldwell, K. S. Novoselov, T. Taniguchi, K. Watanabe, F. Gaussmann, and T. Taubner, Nat. Commun. **6**, 7507 (2015).

[4] A. Cepellotti, G. Fugallo, L. Paulatto, M. Lazzeri, F. Mauri, and N. Marzari, Nat. Commun. **6**, 6400 (2015).

[5] N. Bonini, M. Lazzeri, N. Marzari, and F. Mauri, Phys. Rev. Lett. **99**, 176802 (2007).

[6] I. Jo, M. T. Pettes, J. Kim, K. Watanabe, T. Taniguchi, Z. Yao, and L. Shi, Nano Lett. **13**, 550 (2013).

[7] D. Golla, A. Brasington, B. J. LeRoy, and A. Sandhu, APL Materials **5**, 056101 (2017).

[8] S. Chen, Q. Wu, C. Mishra, J. Kang, H. Zhang, K. Cho, W. Cai, A. A. Balandin, and R. S. Ruoff, Nat. Mater. **11**, 203 (2012).

[9] D. T. Morelli, J. P. Heremans, and G. A. Slack, Phys. Rev. B **66**, 195304 (2002).

[10] A. J. Giles, S. Dai, I. Vurgaftman, T. Hoffman, S. Liu, L. Lindsay, C. T. Ellis, N. Assefa, I. Chatzakis, T. L. Reinecke, J. G. Tischler, M. M. Fogler, J. H. Edgar, D. N. Basov, and J. D. Caldwell, Nat. Mater. **17**, 5047 (2017).

[11] A. Maity, T. C. Doan, J. Li, J. Y. Lin, and H. X. Jiang, Appl. Phys. Lett. **109**, 072101 (2016).

[12] J. Serrano, A. Bosak, R. Arenal, M. Krisch, K. Watanabe, T. Taniguchi, H. Kanda, A. Rubio, and L. Wirtz, Phys. Rev. Lett. **98**, 095503 (2007).

[13] P. Giura, N. Bonini, G. Creff, J. B. Brubach, P. Roy, and M. Lazzeri, Phys. Rev. B **86**, 121404(R) (2012).

[14] R. Cuscó, B. Gil, G. Cassabois, and L. Artús, Phys. Rev. B **94**, 155435 (2016).

[15] T. Q. P. Vuong, S. Liu, A. van de Lee, R. Cuscó, L. Artús, T. Michel, P. Valvin, J. H. Edgar, G. Cassabois, and B. Gil, Nat. Mater. **17**, 5048 (2017).

[16] J. Menéndez and M. Cardona, Phys. Rev. B **29**, 2051 (1984).

[17] N. Domènech-Amador, R. Cuscó, L. Artús, T. Yamaguchi, and Y. Nanishi, Phys. Rev. B **83**, 245203 (2011).

[18] N. Marom, J. Bernstein, J. Garel, A. Tkatchenko, E. Joselevich, L. Kronik, and O. Hod, Phys. Rev. Lett. **105**, 046801 (2010).

[19] K. V. Zakharchenko, M. I. Katsnelson, and A. Fasolino, Phys. Rev. Lett. **102**, 046808 (2009).

[20] H. Rydberg, M. Dion, N. Jacobson, E. Schröder, P. Hyldgaard, S. I. Simak, D. C. Langreth, and B. I. Lundqvist, Phys. Rev. Lett. **91**, 126402 (2003).

[21] G. Kern, G. Kresse, and J. Hafner, Phys. Rev. B **59**, 8551 (1999).

[22] ABINIT is a common project of the Université Catholique de Louvain, Corning Incorporated, and other contributors (http://www.abinit.org). X. Gonze, J.-M. Beuken, R. Caracas, F. Detraux, M. Fuchs, G.-M. Rignanese, L. Sindic, M. Verstraete, G. Zerah, F. Jollet, et al., Comput. Mater. Sci. **25**, 478 (2002).

[23] D. J. Chadi and M. L. Cohen, Phys. Rev. B **8**, 5747 (1973).

[24] N. Mounet and N. Marzari, Phys. Rev. B **71**, 205214 (2005).

[25] J. M. Zhang, T. Ruf, M. Cardona, O. Ambacher, M. Stutzmann, J.-M. Wagner, and F. Bechsted, Phys. Rev. B **56**, 14399 (1997).

[26] A. Göbel, T. Ruf, C.-T. Lin, M. Cardona, J.-C. Merle, and M. Joucla, Phys. Rev. B **56**, 210 (1997).

[27] A. Göbel, T. Ruf, J. M. Zhang, R. Lauck, and M. Cardona, Phys. Rev. B **59**, 2749 (1999).

[28] J. Serrano, F. J. Manjón, A. H. Romero, F. Widulle, R. Lauck, and M. Cardona, Phys. Rev. Lett. **90**, 055510 (2003).

[29] R. Cuscó, E. Alarcón-Lladó, J. Ibáñez, L. Artús, J. Jiménez, B. Wang, and M. J. Callahan, Phys. Rev. B **75**, 165202 (2007).

[30] W. Paszkowicz, J. Pelka, M. Knapp, T. Szyszko, and S. Podsiadlo, Appl. Phys. A **75**, 431 (2002).

[31] B. Yates, M. J. Overy, and O. Pirgon, Philos. Mag. **32**, 847 (1975).

[32] R. P. Feynman, *Statistical Mechanics: A Set of Lectures*, Advanced book classics (Westview Press, Boulder, Colo, 1998).

[33] S. Tamura, Phys. Rev. B **30**, 849 (1984).